J. Fluid Mech. (1978), *vol.* 84, *part* 2, *pp.* 291–303
Printed in Great Britain

Internal electrohydrodynamic instability of liquids with collinear field and conductivity gradients

By JAMES F. HOBURG

Department of Electrical Engineering, Carnegie-Mellon University, Pittsburgh, Pennsylvania 15213

(Received 1 December 1976 and in revised form 6 June 1977)

Bulk-coupled instability at the interface between miscible fluids which have identical mechanical properties but disparate electrical conductivities and are stressed by an equilibrium normal electric field is studied experimentally and theoretically. Observations of fluid motions permit measurement of an instability wavenumber and growth rate.

A model with a layer of diffusive conductivity distribution coupled to uniform bounding half-spaces is developed. Numerical integration of linearized electromechanical equations leads to a set of growing eigenfrequencies with corresponding eigenmodes, pure real for small wavenumber and complex (propagating) for large wavenumber.

The fastest growing wavenumber and corresponding growth rate are characterized as a function of the conductivity ratio and a time-constant ratio, which reflects the importance of inertial and viscous effects. In the viscous-dominated limit, the description agrees with a corresponding surface-coupled theory. The model is evaluated for parameters corresponding to experimental observations.

1. Introduction

Understanding of electrohydrodynamic instability mechanisms at the interface between fluids experiencing an equilibrium normal electric field dates back at least to Rayleigh's (1882) analysis of the stability limit for charge on a conducting drop. More recent work has dealt with instability of a planar layer of liquid stressed by a normal electric field (Taylor & McEwan 1965; Melcher 1963) and instability and breakup of conducting fluid jets and drops in electric fields (Melcher 1963; Taylor 1964).

The dispersion relation for small amplitude motions driven by an initially normal electric field at a plane abrupt interface between two Ohmic fluids has been derived and verified experimentally in some limiting cases (Melcher & Smith 1969). A basic limitation of such a surface-coupled model, with a description of instability dynamics in terms of interfacial motions, has led to investigations of mechanisms on the scale of the thickness of the interface itself. Observation of an electrohydrodynamic instability at the boundary between fluids with identical mechanical properties but differing electrical conductivities in an equilibrium tangential electric field, where the surface-coupled theory predicts no electromechanical coupling, has led to a volume-coupled description, wherein constant-property layers are spliced together through

a layer of varying conductivity (Hoburg & Melcher 1976). This 'transfer relation' method, with inclusion of a numerical integration scheme, has been used to model instability processes underlying mixing from a highly conducting thin layer into a bulk region of smaller uniform conductivity (Hoburg & Melcher 1977). Such bulk-coupled analyses set the stage for the model to be presented here: description of electrohydrodynamic instability at the interface between fluid components experiencing an equilibrium normal electric field, with interfacial structure in the form of a conductivity gradient collinear with the initial field direction.

2. Experimental motivation

Recent experimental studies have compared interfacial displacements as functions of time in a normal electric field with growth rates predicted by the surface-coupled model (Kath & Hoburg 1976). In this context, electrically driven motions on the scale of the interfacial conductivity distribution have been documented. Figure 1 (plate 1) shows a sequence of shadowgraph photographs taken through the same experimental cell with Mazola corn oil, altered in electrical conductivity with anti-static fluid and in colour with red dye, interfaced with the pure liquid. After formation, the interface is permitted to diffuse for a period of 8 min before application of an electric field in the vertical direction. The sequence documents growth of a roughly sinusoidal displacement from the equilibrium position, and hence instability dynamics driven by charge accumulation within the region of varying conductivity. The model to be developed here is aimed towards a description of this configuration in terms of the property structure of the interfacial region.

3. A varying-conductivity layer in a normal electric field: general equations

The distribution of fluid conductivity $\sigma_0(x)$ in a region bounded above and below by constant-conductivity half-spaces, as shown in figure 2, is governed by a one-dimensional diffusion equation with assumed diffusion coefficient κ_d:

$$\partial\sigma_0/\partial t = \kappa_d \partial^2\sigma_0/\partial^2 x. \tag{1}$$

The solution to (1) reaching limiting values $\sigma_0 = \sigma^\alpha$ as $x \to +\infty$ and $\sigma_0 = \sigma^\beta$ as $x \to -\infty$ is

$$\sigma_0(x,t) = \tfrac{1}{2}[(\sigma^\beta + \sigma^\alpha) - (\sigma^\beta - \sigma^\alpha)\,\mathrm{erf}\{x/2(\kappa_d t)^{\frac{1}{2}}\}], \tag{2}$$

or in terms of a normalized conductivity function at time $t = t_0$,

$$h_0' = \frac{\sigma_0}{\sigma^\alpha} = \frac{1+R}{2}\left[1 - \frac{R-1}{R+1}\,\mathrm{erf}\,(x')\right], \tag{3}$$

where $R = \sigma^\beta/\sigma^\alpha$, $x' = x/l_d$ and $l_d = 2(\kappa_d t_0)^{\frac{1}{2}}$. h_0' has a constant value in the half-space bounding fluid regions:

$$h_0' = \begin{cases} 1 & \text{for} \quad x' > c, \\ R & \text{for} \quad x' < -c, \end{cases}$$

where $c \gg 1$ is a number defining the thickness of the region over which (3) must be used to specify the conductivity distribution. In the stability analysis to follow, results are insensitive to the particular value chosen for c.

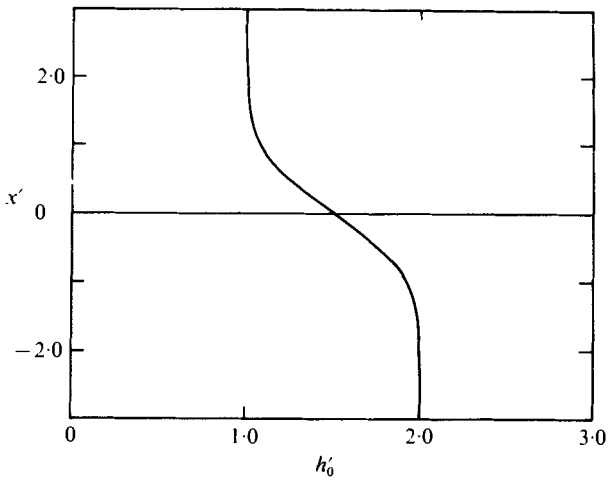

FIGURE 2. Normalized equilibrium conductivity distribution $h_0'(x')$ in varying-conductivity layer for $R = 2$ and $c = 3$.

The general equations governing electromechanical coupling within the region of varying conductivity, with viscous and inertial effects included in the Navier–Stokes relations and a diffusion time long and charge relaxation time short compared with times describing fluid motions, have been written out in previous papers (Hoburg & Melcher 1976, 1977).

4. Determination of layer transfer relations

With the equilibrium electric field collinear with a gradient in the equilibrium conductivity distribution, the perturbation dynamics are governed by a system of six first-order, variable-coefficient differential equations (Hoburg & Melcher 1977). Application of a fourth-order Runge–Kutta method (Greenspan 1971) of numerical integration determines perturbation variables at $x' = c$ in terms of the same variables at $x' = -c$. A set of matrix manipulations, then, results in the elements of a 6×6 transfer matrix $\mathbf{Q}$ defined by

$$\mathbf{S} = \mathbf{Q}\mathbf{V}, \tag{4}$$

where

$$\mathbf{S} \equiv [\hat{S}_x'^{\alpha}, \hat{S}_x'^{\beta}, \hat{S}_z'^{\alpha}, \hat{S}_z'^{\beta}, \hat{J}_x'^{\alpha}, \hat{J}_x'^{\beta}]^T,$$

$$\mathbf{V} \equiv \hat{v}_x'^{\alpha}, \hat{v}_x'^{\beta}, \hat{v}_z'^{\alpha}, \hat{v}_z'^{\beta}, \hat{\phi}'^{\alpha}, \hat{\phi}'^{\beta}]^T.$$

$\hat{S}'$, $\hat{J}'$, $\hat{v}'$ and $\hat{\phi}'$ denote the normalized perturbation stress, current density, velocity and potential respectively, subscripts x and z denote collinear and orthogonal (to the conductivity gradient) components respectively, and superscripts α and β denote variables evaluated at $x' = c$ and $x' = -c$ respectively. The elements of $\mathbf{Q}$ are functions of the normalized growth rate $s' \equiv s\tau$, the normalized wavenumber $k' \equiv kl_d$, R and T/τ, where

$$T \equiv \rho l_d^2/\eta, \quad \tau \equiv \eta/e(E^{\alpha})^2.$$

5. Layer spliced to bounding half-spaces

The fluid regions $x' > c$ and $x' < -c$, above and below the varying-conductivity layer respectively, have no induced perturbation charge in the face of fluid motions. The regions are thus electromechanically 'uncoupled', and may be characterized by purely mechanical and purely electrical transfer relations, as developed in the context of the analogous tangential-field problem (Hoburg & Melcher 1976), with 2×2 transfer matrices $\mathbf{P}^\alpha$ and $\mathbf{P}^\beta$ describing the mechanical relations:

$$\begin{bmatrix} \hat{S}'^{\alpha}_x \\ \hat{S}'^{\alpha}_z \end{bmatrix} = \mathbf{P}^\alpha \begin{bmatrix} \hat{v}'^{\alpha}_x \\ \hat{v}'^{\alpha}_z \end{bmatrix}, \tag{5}$$

$$\hat{J}'^{\alpha}_x = k' \hat{\phi}'^{\alpha}, \tag{6}$$

$$\begin{bmatrix} \hat{S}'^{\beta}_x \\ \hat{S}'^{\beta}_z \end{bmatrix} = \mathbf{P}^\beta \begin{bmatrix} \hat{v}'^{\beta}_x \\ \hat{v}'^{\beta}_z \end{bmatrix}, \tag{7}$$

$$\hat{J}'^{\beta}_x = -Rk' \hat{\phi}'^{\beta}. \tag{8}$$

Splicing the three regions together, then, is accomplished by combining (4)–(8):

$$\mathbf{FV} = [\mathbf{0}], \tag{9}$$

where $\mathbf{0}$ is a column matrix of six zeros and

$$\mathbf{F} = \begin{bmatrix} Q_{11}-P^\alpha_{11} & Q_{12} & Q_{13}-P^\alpha_{12} & Q_{14} & Q_{15} & Q_{16} \\ Q_{21} & Q_{22}-P^\beta_{11} & Q_{23} & Q_{24}-P^\beta_{12} & Q_{25} & Q_{26} \\ Q_{31}-P^\alpha_{21} & Q_{32} & Q_{33}-P^\alpha_{22} & Q_{34} & Q_{35} & Q_{36} \\ Q_{41} & Q_{42}-P^\beta_{21} & Q_{43} & Q_{44}-P^\beta_{22} & Q_{45} & Q_{46} \\ Q_{51} & Q_{52} & Q_{53} & Q_{54} & Q_{55}-k' & Q_{56} \\ Q_{61} & Q_{62} & Q_{63} & Q_{64} & Q_{65} & Q_{66}+Rk' \end{bmatrix}. \tag{10}$$

For non-trivial solutions to (9), the dispersion relation takes the form

$$D = \det \mathbf{F} = 0. \tag{11}$$

An eigenfrequency s', then, is a value of s' satisfying (11) for given R, T/τ and k'. A search in the complex s' plane for zeros of the function $D(s)$ is carried out according to a procedure described by Betchov & Criminale (1967).

The function $D(s')$ has complex-conjugate symmetry about the real s' axis (i.e. $D(s'_r + is'_i)$ is the complex conjugate of $D(s'_r - is'_i)$) and hence only a search for zeros in the upper half-plane need be carried out. In general, an infinite set of growing (positive real part) eigenfrequencies may be expected (each with its corresponding distribution of physical quantities, i.e. eigenfunctions). Attention is here focused on the two fastest growing eigenfrequencies, whose nature depends on the value chosen for k', as shown in figure 3. Both zeros of $D(s')$ start at the origin when $k' = 0$ then, with increasing k', take on positive, pure-real values. The fastest growing eigenfrequency reaches a maximum at a value of k' termed k'^*, then decreases to meet the still rising second eigenfrequency. At this value of k', the two distinct zeros merge on the real axis, and with further increases in k' become a conjugate pair in the complex s' plane. Thus the solid line in figure 3 for large k' represents $\mathrm{Re}\, s'$ and the dashed line $\pm \mathrm{Im}\, s'$.

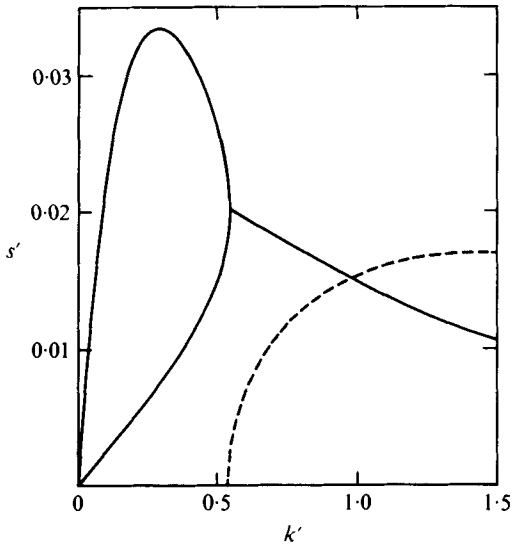

FIGURE 3. Instability growth rate s' *vs.* wavenumber k' for the two fastest growing eigenfrequencies, with $R = 2$ and $T/\tau = 1$. ——, real part; – – –, imaginary part. Both eigenfrequencies are pure real for small k', but merge to form a complex-conjugate pair for large k'. The largest value of s' and the corresponding k' are termed s'^* and k'^* respectively.

6. Eigenfunctions: potential and velocity distributions

Insight into the significance of the eigenfrequencies may be gained by plotting the distributions of physical quantities as functions of the vertical (x) co-ordinate. For a known value of s' where (11) is satisfied, linear combinations of rows of **F** are taken so as to produce zeros everywhere below the main diagonal. Then, because $D(s') = 0$, the (6,6) element will become zero. Thus $\hat{\phi}'^{\beta}$ may be arbitrarily set to the value $1 + i0$. The manipulated set of equations derived from (10) then determines values of the other variables in **V**. In turn, (5)–(8) determine the values of variables in **S**. Knowledge of the six β variables $\hat{v}_x'^{\beta}$, $\hat{v}_z'^{\beta}$, $\hat{\phi}'^{\beta}$, $\hat{S}_x'^{\beta}$, $\hat{S}_z'^{\beta}$ and $\hat{J}_x'^{\beta}$ allows a numerical integration of the governing differential equations to determine the distribution of each quantity across the layer. Upon arrival at the α surface, the values obtained for the six variables are compared with the values specified by entries in **V** and **S** as a check on the validity of the eigenfrequency solution to (11). Distributions of physical quantities in the bounding half-spaces are determined by the uncoupled equations which led to the half-space transfer relations (5)–(8). Figures 4–6 are plots of distributions of the potential $\hat{\phi}'$ and normal velocity $\hat{v}_x'$ across the varying-conductivity layer and one layer thickness into each bounding half-space. Figure 4 shows eigenfunctions at the fastest growing eigenfrequency $s' = s'^*$, at $k' = k'^*$, for $R = 2$ and $T/\tau = 1$. Figure 5 shows eigenfunctions at the second eigenfrequency, also at $k' = k'^*$. Finally, in figure 6, k' has been increased to 1, where the eigenfrequency is complex, and the corresponding physical quantities have the real and imaginary parts denoted by the solid and dashed lines. As is typical of eigenfunction distributions, less rapidly growing eigenfrequencies involve more rapid spatial variation of physical quantities.

The nature of the perturbation quantities at the fastest growing eigenfrequency is clarified by a comparison with corresponding quantities in the surface-coupled model

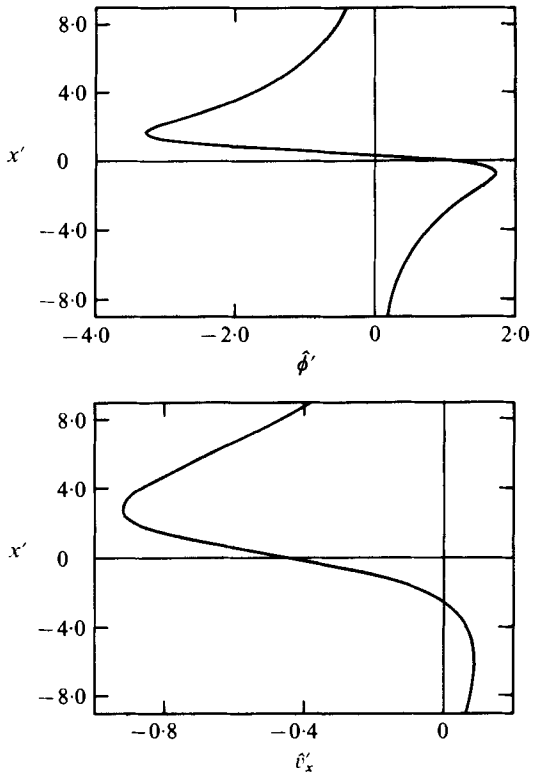

FIGURE 4. Eigenfunctions $\hat{\phi}$ and $\hat{v}'_x$ at the fastest growing eigenfrequency $s^* = 0{\cdot}0336$ with $R = 2$ and $T/\tau = 1$.

(Melcher & Smith 1969; Kath & Hoburg 1977) at corresponding parameter values, as shown in figure 7. The discontinuity in $\hat{\phi}'$ at the abrupt surface represents a discontinuity in the tangential electric field driven by the perturbation normal velocity $\hat{v}'_x$ and the equilibrium electric field:

$$\hat{\phi}'^{\alpha} - \hat{\phi}'^{\beta} = 2\hat{v}'^{\alpha}_x/(1 - R^{-1})s'. \tag{12}$$

The perturbation potential outside the varying-conductivity region and the perturbation normal velocity throughout are quite similar in the bulk-coupled and surface-coupled representations of figures 4 and 7 respectively. As expected, the surface-coupled $\hat{v}'_x$ is slightly increased in magnitude near the surface and slightly decreased away from the surface. Like the corresponding fastest growing normal-velocity eigenfunction in the equilibrium orthogonal-field problem (Hoburg & Melcher 1976), $\hat{v}'_x$ changes sign near the interface. Unlike the corresponding equilibrium orthogonal-field potential eigenfunction, $\hat{\phi}$ also changes sign near the interface, consistent with a discontinuity in the surface-coupled description as given by (12).

Further insight is gained by plotting fluid streamlines corresponding to velocity distributions. In figure 8, streamlines corresponding to the velocity distribution in figure 4, i.e. at k'^* and s'^*, are plotted. Fluid motions are more extensive in the upper (less-conducting) half-space, and form a cellular pattern corresponding to the assumed periodicity in the z direction, with a structure similar to corresponding streamlines

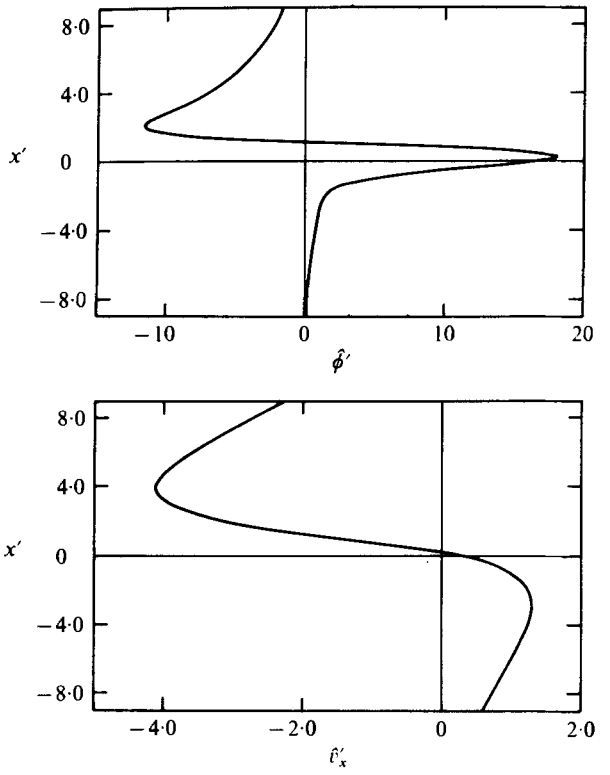

FIGURE 5. Eigenfunctions $\hat{\phi}$ and $\hat{v}'_x$ at the second fastest growing eigenfrequency $s' = 0{\cdot}00753$ at k'^* with $R = 2$ and $T/\tau = 1$.

in the surface-coupled model (Kath & Hoburg 1977). The physical effect represented here, then, is a sweeping of fluid up from the layer into the less-conducting half-space every wavelength, and back down a half-wavelength away. In figure 9, the streamlines correspond to the figure 6 velocity distribution at $k' = 1$. Here, with a complex eigenfrequency, the cellular pattern becomes a series of slanted layers, propagating in the z direction. The physical mechanism associated with this mode is similar to that responsible for instability in the structured tangential-field model (Hoburg & Melcher 1976), with charge accumulation and cellular motions leading to propagation. With the change in the direction of the equilibrium field comes a reversal in the relationship of propagation and streamline slant directions, consistent with the mechanism described.

7. Dependence on conductivity and time-constant ratios

The behaviour of the fastest growing eigenfrequency s'^* and corresponding wavenumber k'^* as functions of the parameters R and T/τ is described by figures 10–13. In figures 10 and 11, k'^* and s'^* are plotted as functions of T/τ on a logarithmic scale for three values of R. Note the relative insensitivity of both quantities to T/τ over a wide range. If T/τ is increased by increasing E^α, k^* increases slowly while s^* increases less rapidly than quadratically with E^α. Alternatively, if T/τ is increased by increasing

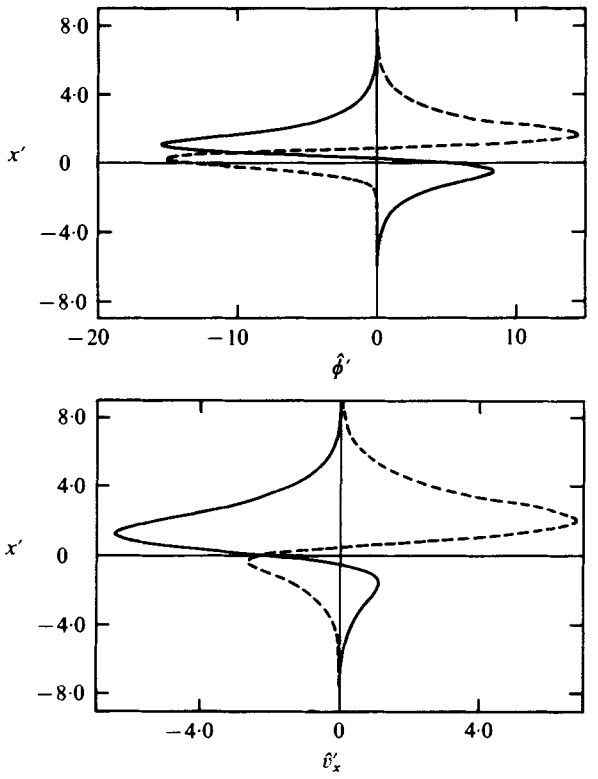

FIGURE 6. Complex eigenfunctions $\hat{\phi}'$ and $\hat{v}'_x$ at the fastest growing eigenfrequency at $k' = 1$ with $R = 2$ and $T/\tau = 1$. ——, real part; – – –, imaginary part.

l_d, k^* decreases less rapidly than $1/l_d$ and s^* also decreases. Thus increasing inertial effects at constant R increases the fastest growing wavenumber, i.e. decreases the scale of the motion, reflecting the balance between viscous and inertial drag. The corresponding fastest growth rate decreases with addition of inertia.

Figures 12 and 13 display k'^* and s'^* as functions of R for four values of T/τ. Increasing R increases k'^* and s'^*, in a manner very insensitive to R. Sensitivity to R increases with increasing inertia. Finally, the relevance of a surface-coupled analysis to the description at hand is made clear by considering the limit as $T/\tau \to 0$. In turn, k'^* becomes increasingly small (see figures 10 and 12), i.e. the fastest growing disturbance occurs at a wavelength long enough to make the layer have the same effect as an abrupt interface. Correspondingly, the 'viscous-dominated' regime of the surface-coupled analysis (Kath & Hoburg 1977) has a growth rate defined by

$$s = \frac{1}{2\tau_E} = \frac{\epsilon J_0^2}{4\eta}\left[\frac{1}{\sigma^\alpha} - \frac{1}{\sigma^\beta}\right]^2. \tag{13}$$

Thus normalizing gives

$$s' = s\tau = \tfrac{1}{4}[1 - R^{-1}]^2. \tag{14}$$

Equation (14) produces the curve labelled 'surface-coupled limit' on figure 13, a limiting growth rate approached by the bulk-coupled analysis as inertial effects become negligible.

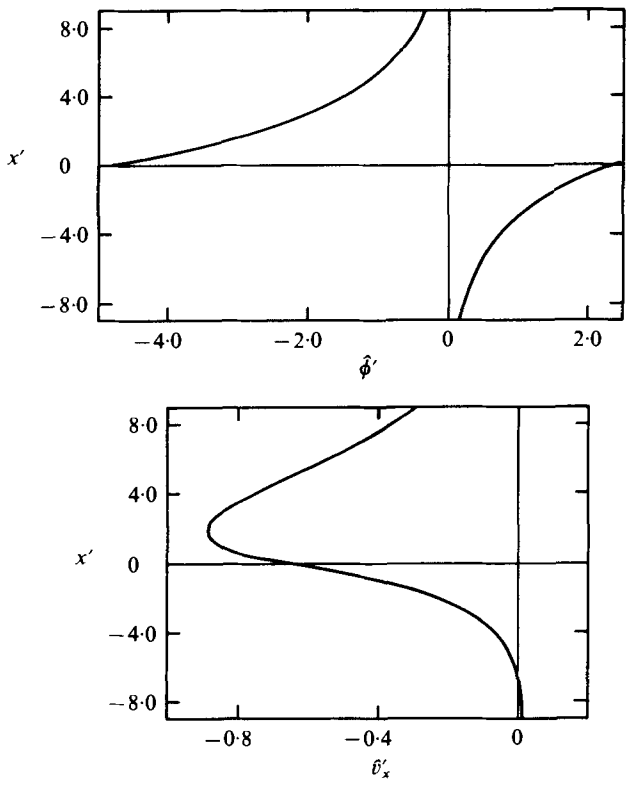

FIGURE 7. Eigenfunctions $\hat{\phi}'$ and $\hat{v}_x'$ as determined by surface-coupled theory at parameter values corresponding to $R = 2$ and $T/\tau = 1$.

8. Correspondence between theory and experiment

The sequence of shadowgraph photographs shown in figure 1 affords an opportunity to test the applicability of the model described in §§3–7. A sinusoidal displacement of the broadened interfacial structure from the equilibrium position permits an experimental determination of the wavenumber and growth rate. Growth proceeds roughly exponentially through the sequence, and hence the experimental growth rate is determined by the slope of a line joining points on a plot of ln (displacement/displacement at $t = 0$) *vs.* time. The wavenumber is inferred directly from the observed wavelength. The values read from figure 1 are

$$s_{\text{exp}} = 0{\cdot}76\,\text{s}^{-1}, \quad k_{\text{exp}} = 269\,\text{m}^{-1}.$$

The values of the material parameters and electric field for the corn-oil experiment shown are

$$\rho = 0{\cdot}94 \times 10^3\,\text{kg/m}^3,$$

$$\eta = 5{\cdot}46 \times 10^{-2}\,\text{kg/ms},$$

$$\epsilon = 3{\cdot}1\,\epsilon_0 = 2{\cdot}74 \times 10^{-11}\,\text{F/m},$$

$$R = 2,$$

$$E^{\alpha} = 1{\cdot}91 \times 10^5\,\text{V/m}.$$

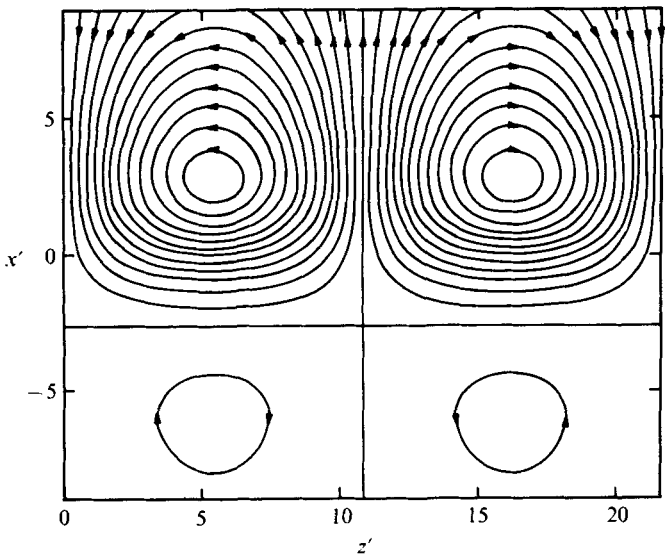

FIGURE 8. Fluid streamlines corresponding to velocity eigenfunction in figure 4, at s'^* with $R = 2$ and $T/\tau = 1$. The cellular pattern takes the form of a standing wave, with fluid motions more extensive in the upper (less-conducting) half-space.

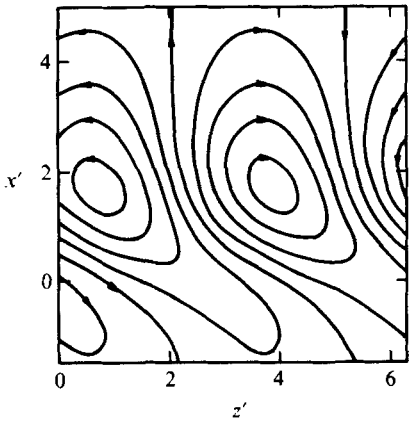

FIGURE 9. Fluid streamlines corresponding to complex velocity eigenfunction in figure 6, at $k' = 1$ with $R = 2$ and $T/\tau = 1$.

Because the diffusion length l_d is not known, it is not possible to compute k' or T/τ directly. However, only one value of l_d can produce values for k'^* and T/τ corresponding to the appropriate curve in figure 10. Thus, by iteratively guessing values for l_d to use in computing k'^* and T/τ, a point on the $R = 2$ curve consistent with both relations is determined. This point is at

$$T/\tau = 0{\cdot}168, \quad k'^* = 0{\cdot}197$$

with $l_d = 7{\cdot}30 \times 10^{-4}$ m. In turn, reading off the value of s'^* for the T/τ determined from figure 11 gives

$$s'^* = 0{\cdot}044,$$

or

$$s^* = 0{\cdot}81\,\mathrm{s}^{-1}.$$

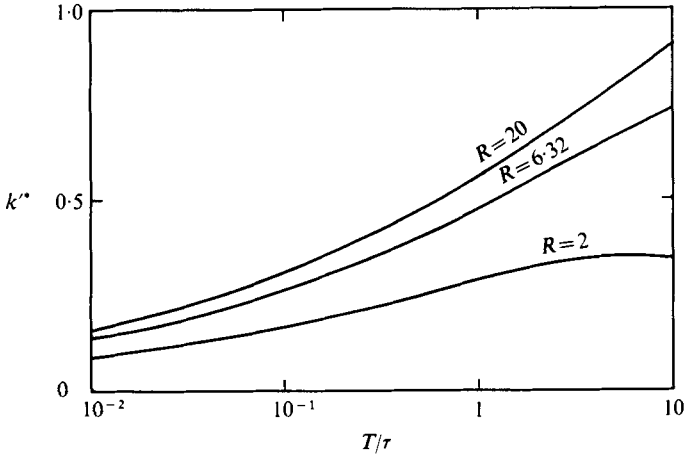

FIGURE 10. k'^* *vs.* T/τ at constant values of R.

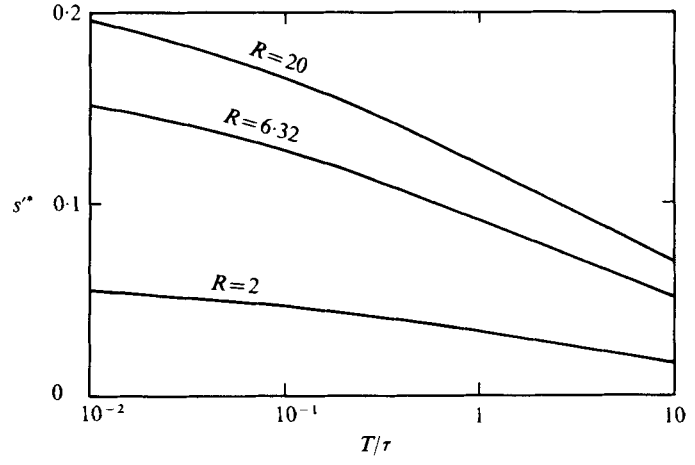

FIGURE 11. s'^* *vs.* T/τ at constant values of R.

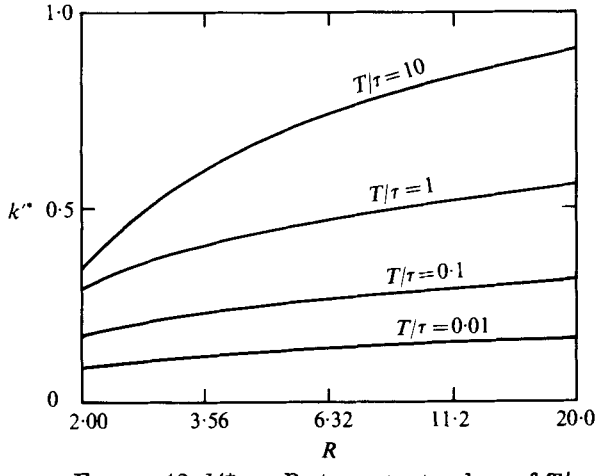

FIGURE 12. k'^* *vs.* R at constant values of T/τ.

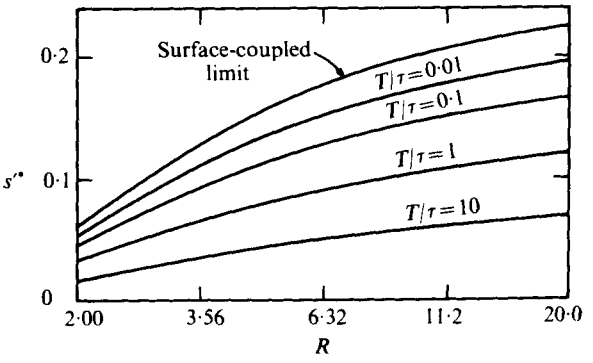

FIGURE 13. s'^* *vs.* R at constant values of T/τ. As $T/\tau \to 0$, the dependence approaches that predicted by a surface-coupled model.

The good correspondence of this value of s^*, determined through the bulk-coupled theory using a measured wavenumber, with the directly measured growth rate provides evidence of the descriptive relevance of the model to the experiment.

It is not possible, using experimental documentation of the kind shown in figure 1, to claim direct evidence of cellular fluid motions corresponding to those shown in figure 8, where it is clear that considerably more fluid motion occurs in the less-conducting region. No mechanism for visualizing the flow pattern outside the varying-property region has been built into the experiment. The same is true of analogous work connecting surface-coupled theory and experiments, where the model predicts a high concentration of fluid motions in the less-conducting material: directly obtainable experimental evidence comes in terms of the evolution in time of interfacial motions. Comparison of the velocity amplitudes in figures 4 and 7 emphasizes the point that the structure of fluid motions in the bulk-coupled model, even through the variable-property region, is quite similar to that predicted by the surface-coupled model. Motion on the scale of the interfacial region is difficult to observe because, in correspondence with the determined most critical wavenumber k'^*, the instability wavelength is about 32 times as long as the diffusion length l_d. The most direct manifestation of interfacial structure comes in terms of a decrease in the predicted and observed growth rate.

9. Conclusions

The model and experiment described here extend the understanding of instability at the interface between fluid components of differing electrical conductivities stressed by an equilibrium normal electric field to include coupling mechanisms 'within the interface', i.e. bulk-coupled interactions driven by accumulation of volume free charge density in a region where a collinear conductivity gradient and electric field appear. As such, it forms the logical conclusion to a series of recent descriptions of volume-coupled phenomena occurring in geometries traditionally modelled in terms of interfacial motions driven by surface force densities. Although the methods involved in describing volume- and surface-coupled phenomena differ considerably, the resulting predictions, in terms of fluid motions and the instability growth rate, agree exactly

in the appropriate limit, and are quite similar even with broadened interfacial structure, with a decreasing growth rate the most significant result of increasing diffusion length.

Interactions of the kind described here are of practical importance in operations where an electric field is used to drive fluid mixing on a fine scale, where mechanical means are inefficient (Hoburg & Melcher 1977). Recent experiments in an apparatus designed to produce shear deformation between viscous fluid components to be mixed have demonstrated augmentation of performance with application of an electric field across the streamline component structure (Rotz 1976). The analysis presented here relates directly to the electrically driven instability responsible for such interactions.

Mr Farrokh Malihi took the ciné film which provided the sequence of photographs in figure 1. This work was supported by NSF Grant ENG76-09246.

REFERENCES

BETCHOV, R. & CRIMINALE, W. O. 1967 *Stability of Parallel Flows*, p. 78. Academic Press.

GREENSPAN, D. 1971 *Introduction to Numerical Analysis and Applications*, pp. 114–116. Markham.

HOBURG, J. F. & MELCHER, J. R. 1976 Internal electrohydrodynamic instability and mixing of fluids with orthogonal field and conductivity gradients. *J. Fluid Mech.* **73**, 333–351.

HOBURG, J. F. & MELCHER, J. R. 1977 Electrodydrodynamic mixing and instability induced by collinear fields and conductivity gradients. *Phys. Fluids* **20**, 903–911.

KATH, G. S. & HOBURG, J. F. 1977 Interfacial electrohydrodynamic instability in normal electric field. *Phys. Fluids* **20**, 912–916.

MELCHER, J. R. 1963 *Field-Coupled Surface Waves*, chap. 6. M.I.T. Press.

MELCHER, J. R. 1972 Electrohydrodynamics. *Appl. Mech. Proc. 13th Int. Cong. Theor. Appl. Mech., Moscow*, pp. 240–263. Springer.

MELCHER, J. R. & SMITH, C. V. 1969 Electrohydrodynamic charge relaxation and interfacial perpendicular-field instability. *Phys. Fluids* **12**, 778–790.

RAYLEIGH, LORD 1882 On the equilibrium of liquid conducting masses charged with electricity. *Phil. Mag.* **14**, 184–186.

ROTZ, C. 1976 A generalized approach to increased mixing efficiency for viscous liquids. S.M. thesis, Dept. of Mech. Eng., M.I.T.

TAYLOR, G. I. 1964 Disintegration of water drops in an electric field. *Proc. Roy. Soc.* **280**, 383–397.

TAYLOR, G. I. & MCEWAN, A. D. 1965 The stability of a horizontal fluid interface in a vertical electric field. *J. Fluid Mech.* **22**, 1–55.

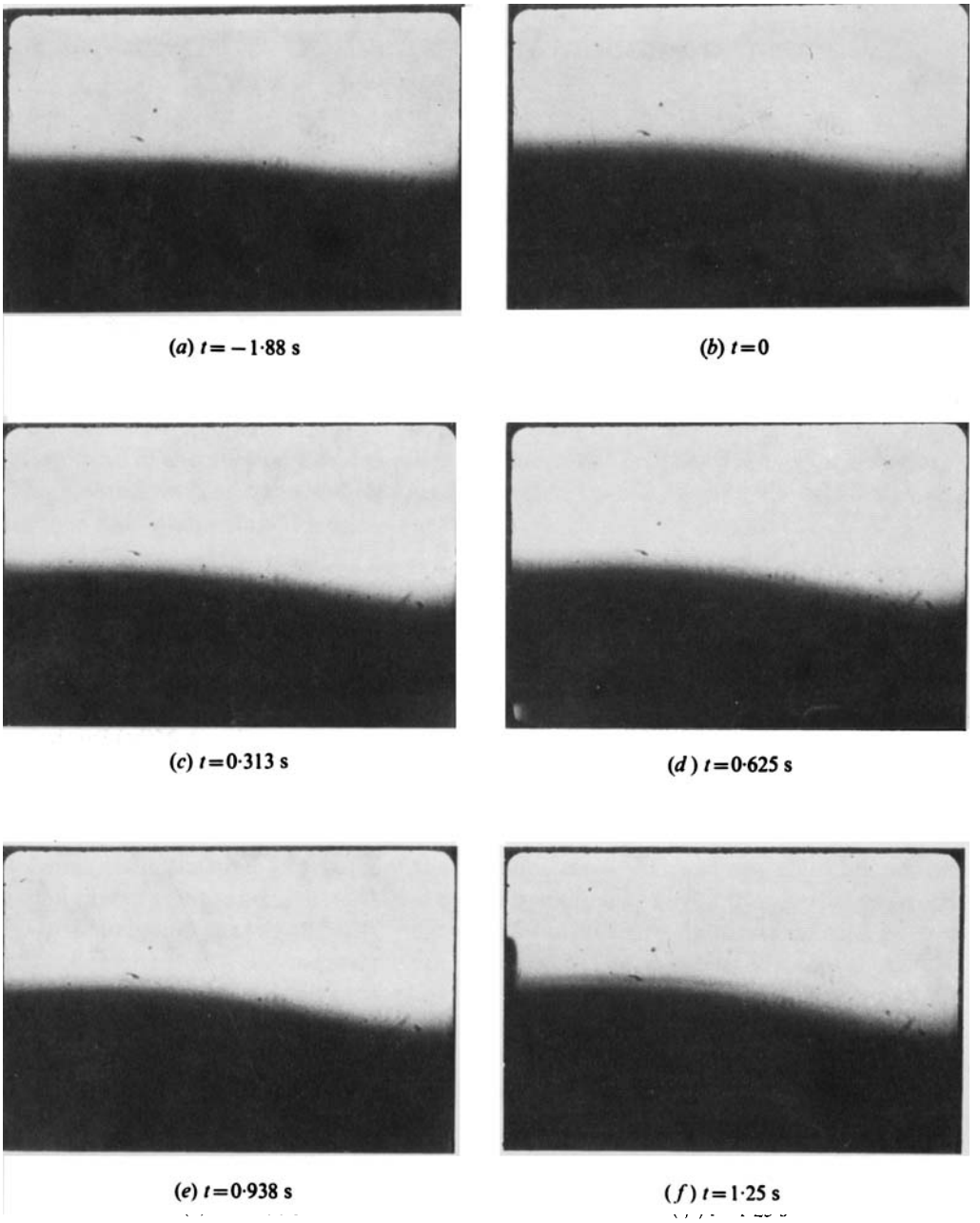

FIGURE 1. Shadowgraph photographs of fluid-component distributions in experimental cell. The lower fluid is more conducting, and the interface has diffused for 8 min after formation. The instability dynamics are driven by charge accumulation within the region of varying conductivity in an equilibrium vertical electric field. A roughly sinusoidal displacement permits measurement of the wavelength and growth rate. The electric field is applied at $t = 0$ [frame (*b*)].